"Soft" oxidative coupling of methane to ethylene: Mechanistic insights from combined experiment and theory

Shanfu Liu[a,b], Sagar Udyavara[c], Chi Zhang[d,e], Matthias Peter[a,b], Tracy L. Lohr[a,b], Vinayak P. Dravid[d,e], Matthew Neurock[c,1], and Tobin J. Marks[a,b,1]

[a]Department of Chemistry, Northwestern University, Evanston, IL 60208; [b]Center for Catalysis and Surface Science, Northwestern University, Evanston, IL 60208; [c]Department of Chemical Engineering and Materials Science, University of Minnesota, Minneapolis, MN 55455; [d]Department of Materials Science and Engineering, Northwestern University, Evanston, IL 60208; and [e]Materials Research Center, Northwestern University, Evanston, IL 60208

Contributed by Tobin J. Marks, April 16, 2021 (sent for review June 18, 2020; reviewed by Alexis T. Bell and Joachim Sauer)

The oxidative coupling of methane to ethylene using gaseous disulfur ($2CH_4 + S_2 \rightarrow C_2H_4 + 2H_2S$) as an oxidant (SOCM) proceeds with promising selectivity. Here, we report detailed experimental and theoretical studies that examine the mechanism for the conversion of CH_4 to C_2H_4 over an Fe_3O_4-derived FeS_2 catalyst achieving a promising ethylene selectivity of 33%. We compare and contrast these results with those for the highly exothermic oxidative coupling of methane (OCM) using O_2 ($2CH_4 + O_2 \rightarrow C_2H_4 + 2H_2O$). SOCM kinetic/mechanistic analysis, along with density functional theory results, indicate that ethylene is produced as a primary product of methane activation, proceeding predominantly via CH_2 coupling over dimeric S–S moieties that bridge Fe surface sites, and to a lesser degree, on heavily sulfided mononuclear sites. In contrast to and unlike OCM, the overoxidized CS_2 by-product forms predominantly via CH_4 oxidation, rather than from C_2 products, through a series of C–H activation and S-addition steps at adsorbed sulfur sites on the FeS_2 surface. The experimental rates for methane conversion are first order in both CH_4 and S_2, consistent with the involvement of two S sites in the rate-determining methane C–H activation step, with a CD_4/CH_4 kinetic isotope effect of 1.78. The experimental apparent activation energy for methane conversion is 66 ± 8 kJ/mol, significantly lower than for CH_4 oxidative coupling with O_2. The computed methane activation barrier, rate orders, and kinetic isotope values are consistent with experiment. All evidence indicates that SOCM proceeds via a very different pathway than that of OCM.

catalysis | sulfur oxidative coupling of methane (SOCM) | kinetics and density functional theory (DFT) | reaction mechanism

The oxidative coupling of methane (OCM) with O_2 would seem to be a concise, direct route to convert methane, one of the most Earth-abundant carbon sources (1), to ethylene ($2CH_4 + O_2 \rightarrow C_2H_4 + 2H_2O$), a key chemical intermediate (2, 3), and this process has been extensively studied (1, 4–19) since 1982 (20). Nevertheless, the widespread use of OCM is challenged by methane overoxidation to CO_2 and other oxygenates. Furthermore, the severe reaction conditions of nonoxidative pathways (2, 21–28) typically risk carbon deposition and catalyst deactivation (2, 21–26). In preliminary studies, we reported a $2CH_4 + S_2 \rightarrow C_2H_4 + 2H_2S$ coupling process that moderates the methane overoxidation driving force using gaseous disulfur (S_2) as a "soft" oxidant (SOCM; Fig. 1*A*) (29). S_2 is isoelectronic with O_2, the major sulfur vapor species at 700 to 925 °C (30–32), and is a less aggressive oxidant than O_2 (33). In this scenario, elemental sulfur is recovered from the H_2S coproduct via the known Claus process (Fig. 1*B*) (30), in a cycle where sulfur mediates/moderates the high nonselective O_2 reactivity. SOCM achieved promising ethylene selectivity, raising intriguing mechanistic questions and the possibility of higher selectivity. Methane + $S_{2(g)}$ ethylene selectivities near ∼20% are achieved over a PdS/ZrO_2 catalyst (29), and oxide precatalysts give selectivities near 33% (34).

Nevertheless, in contrast to extensive OCM (17, 35–39) and nonoxidative CH_4 coupling studies (40), far less is known about the SOCM reaction pathway. Post-SOCM X-ray photoelectron spectroscopy (XPS), X-ray diffraction (XRD), and elemental analysis (29, 34) indicate that the oxide precatalysts are predominantly sulfided. Density functional theory (DFT) analyses of molybdenum sulfide catalysts suggest that methane is activated at M–S or S–S sites to form surface-bound CH_3* species which dehydrogenate to form CH_2* (methylidene) species, which then couple to produce C_2H_4. It was proposed that CH_3* species can also desorb as methyl radicals which couple to form ethane (29). The overoxidation product, CS_2, was suggested to form via sulfur addition to methylidene surface intermediates (29).

Kinetic, mechanistic, and theoretical analyses are needed to better understand the CH_4 conversion pathways to C_2H_4 and other products. In principle, there are two plausible pathways following methane activation: 1) H abstraction from adsorbed methyl species forms methylidene (CH_2*) and methylidyne (CH*) species then couple to C_2 products or undergo oxidation to CS_2 or 2) coupling of surface or gas phase methyl species form ethane, which then dehydrogenates to form ethylene or oxidizes to CS_2. For further SOCM optimization it is important to determine which pathways

Significance

Highly abundant methane is vastly underutilized as a feedstock for chemicals and fuels reflecting its inertness. One seemingly attractive approach to methane utilization would be direct catalytic oxidative coupling of methane (OCM) with O_2 to produce ethylene, a valuable chemical feedstock. However, the exothermicity leads largely to nonselective oxidation to CO_2, a challenge that remains despite decades of research. These results raise the intriguing question of whether the "softer" isoelectronic oxidant, S_2, might achieve analogous SOCM with acceptable selectivity. Here, we report a combined experimental and computational investigation of the SOCM reaction mechanism, comparing and contrasting with that of conventional OCM. We find that SOCM shows promising selectivity to ethylene and proceeds via a very different pathway than does OCM.

Author contributions: S.L., S.U., C.Z., M.P., T.L.L., V.P.D., M.N., and T.J.M. designed research; S.L., S.U., C.Z., M.P., and M.N. performed research; S.L., S.U., C.Z., M.P., and M.N. analyzed data; and S.L., S.U., M.P., V.P.D., M.N., and T.J.M. wrote the paper.

Reviewers: A.T.B., University of California Berkeley; and J.S., Humboldt University.

The authors declare no competing interest.

[1]To whom correspondence may be addressed. Email: mneurock@umn.edu or t-marks@northwestern.edu.

This article contains supporting information online at https://www.pnas.org/lookup/suppl/doi:10.1073/pnas.2012666118/-/DCSupplemental.

Published May 31, 2021.

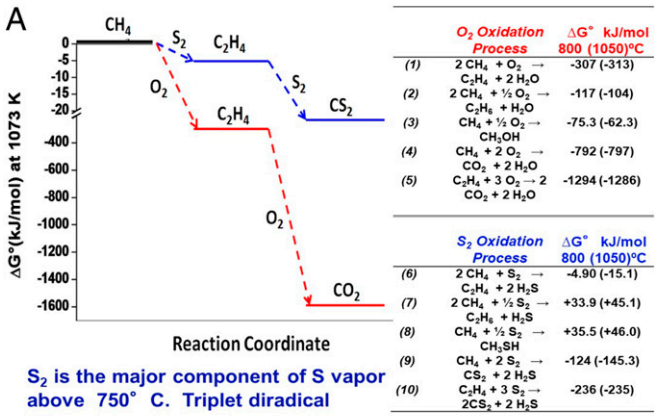

B Claus commercial process

$$2H_2S + 3O_2 = 2SO_2 + 2H_2O$$
$$2H_2S + SO_2 = 3S + 2H_2O$$

Fig. 1. Energetic comparison between the oxidative coupling of methane with O_2 (OCM) and with S_2 (SOCM) and the pathway to recover elemental sulfur from H_2S. (*A*) Gibbs free energy of desired and overoxidation processes in OCM and SOCM at 800 and 1,050 °C. (*B*) Industrialized catalytic Claus process used to recover elemental sulfur from H_2S.

are operative, their relative rates, and the C_2 and CS_2 formation sites.

Here we investigate SOCM pathways over a sulfided Fe_3O_4 precatalyst which affords C_2H_4 selectivities near 33%, complete oxide to sulfide conversion, minimal carbon deposition (coking), and 48-h SOCM stability at 950 °C (34). We first summarize SOCM phenomenology, followed by analysis of the Fe phases during sulfurization and SOCM. Next, kinetic/mechanistic studies focus on the methane and S_2 reaction orders, activation energetics, and isotope effects and probe the pathways governing C_2 vs. CS_2 formation. Complementary DFT calculations focus on reaction mechanisms, the active sites, and their role in product formation. The results are used in a microkinetic model to simulate reaction rates, apparent activation barriers, and reaction rate orders and to compare with experiment. Finally, SOCM and OCM are compared, revealing that they follow distinctly different pathways.

Results

Sulfur Oxidative Coupling of Methane: Phenomenology and Procedures. Catalytic runs begin by exposing the Fe_3O_4 precatalyst to flowing H_2S (sulfurization) for several hours to produce the active catalyst. Catalytic experiments flow Ar over molten S_8 (melting point = 388 K; boiling point = 718 K) to transport gaseous S_2 and a CH_4 into the reactor described previously (29, 34, 41, 42). Gaseous products are quantified by gas chromatography. The primary SOCM reaction products are ethylene and CS_2, with minor amounts of ethane and acetylene. The Fe catalyst exhibits stable selectivity and conversion over the kinetic measurements in the catalytic regime, and methane conversion increases linearly with contact time. More details are provided in *SI Appendix*. The catalyst is characterized by powder XRD (pXRD), scanning and transmission electron microscopy (SEM and TEM), XPS, and Raman spectroscopy (discussed below).

Catalyst Characterization. After Fe_3O_4 sulfurization, the predominant phase detected by pXRD is FeS (Fig. 2*A*) (43, 44). These data differ slightly from our earlier report (34), reflecting improved instrumentation. The Fe 2p3 XPS (Fig. 2*B*) exhibits an intense peak at binding energy (BE) = 707.2 eV, assignable to

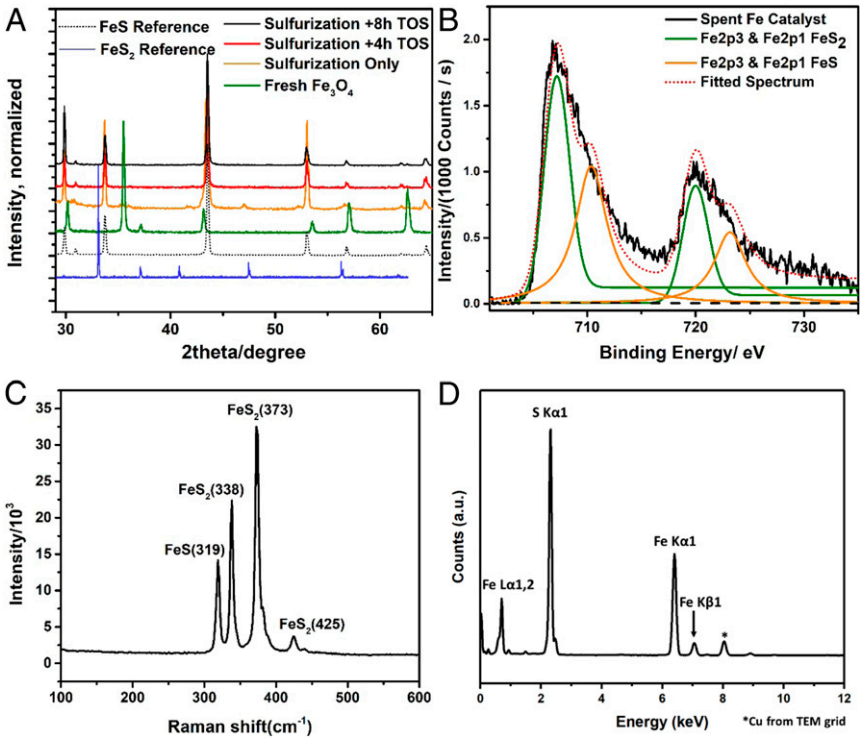

Fig. 2. Characterization of fresh and spent SOCM catalysts. (*A*) pXRD scans of fresh Fe_3O_4 precatalyst (green), sulfurized Fe catalyst (orange), sulfurized Fe catalyst after 4-h catalytic operation (red), and sulfurized Fe catalyst after 8-h catalytic operation (black). References: FeS [black dotted line (43)], FeS_2 [blue solid line (45)]. (*B*) Fe 2p XPS spectra of spent 8-h Fe catalyst after operation at 865 °C, WHSV = 0.785 h^{-1}, and CH_4:S_2 ratio = 1.099. (*C*) Raman spectrum of a Fe SOCM catalyst. Excitation wavelength = 532 nm, sulfurized for 4 h at 865 °C, WHSV of 0.785 h^{-1}. (*D*) EDS spectrum of a selected particle area on an SOCM catalyst after sulfurization for 6 h. The Fe:S ratio = 1:2. a.u., arbitrary units.

FeS_2 [707.3 eV (45)], along with a weaker peak at BE = 710.4 eV assignable to FeS [710.3 eV (46)]. The Raman spectra (Fig. 2*C*) confirm the presence of both crystalline FeS (ν = 319 cm^{-1}) (47) and FeS_2 (ν = 338, 373, and 425 cm^{-1}) (48). The ~5-cm^{-1} deviation from the literature FeS_2 features (48) is consistent with nanocrystallites (49–51), explaining why FeS_2 is not obvious in the pXRD. TEM, selected area electron diffraction, reveal (*SI Appendix*, Fig. S3), in addition to FeS, diffraction patterns along the [001], [102], and [012] zone axes of some particles (*SI Appendix*, Fig. S3) indexed as FeS_2 (space group $Pa\bar{3}$). Energy-dispersive X-ray spectroscopy (EDS) confirms an Fe:S = 1:2 FeS_2 composition (*SI Appendix*, Fig. S4 and Fig. 2*D*). These results show that the Fe_3O_4 precatalyst undergoes sulfurization to generate bulk FeS and likely surface FeS_2. The SOCM performance is stable with time on stream (TOS) up to at least 48 h at 950 °C (34, 52).

Optimum Temperature Range for SOCM Kinetic Data Collection. As shown in *SI Appendix*, Fig. S1, the SOCM Arrhenius plot slope for methane conversion is discontinuous above ~900 °C, implying a change in mechanism, and that the reaction becomes significantly diffusion-limited/noncatalytic at >900 °C (53). Thus, the kinetic measurements were conducted below 865 °C.

The apparent S_2 and methane rate orders were determined from the changes in methane conversion rate as a function of the S_2 and methane pressures, respectively (41, 42). Note these empirical orders are overall apparent orders averaged over the various reaction network pathways (discussed below). The S_2 order was determined using excess CH_4 under pseudo-first-order conditions (see *SI Appendix*), and the measured reaction rates are directly proportional to [S_2] (*SI Appendix*, Figs. S6 and S7). Plotting the ln [methane conversion rate] vs. ln [S_2] indicates that the rate is first-order in [S_2]. A similar approach of plotting ln [methane conversion rate] vs. ln [CH_4] (*SI Appendix*, Figs. S6 and S7) resulted in the linear dependence on [CH_4], indicating that the rate is first-order in [CH_4]. Potential SOCM inhibition effects were also assessed by determining the H_2S and CS_2 reaction orders in excess CH_4 at 865 °C and yield near-zero-order plots (*SI Appendix*, Fig. S5), indicating that CS_2 and H_2S are not significant inhibitors under these conditions.

Reaction Kinetics: Apparent Activation Energetics and Kinetic Isotope Effect. Apparent SOCM activation energies (E_{act}) were determined from Arrhenius plots over 835 to 865 °C. Conversions were held at 5 to 8% and CH_4/S_2 = 1.099, yielding E_{act} = 66 ± 8 kJ/mol, representing an average over the various reaction network pathways. Similar analyses yield activation energies of 85 ± 2 kJ/mol and 39 ± 4 kJ/mol for ethylene and CS_2 formation, respectively (see *SI Appendix*, Table S3). As discussed in *Theoretical Analysis of the SOCM Reaction Mechanism* below, the apparent E_{act} for methane activation reflects the heat of adsorption to form active sulfur sites along with the intrinsic barrier for rate-limiting C–H bond activation. Kinetic isotope effect (KIE) data were acquired from the consumption rate of CH_4 vs. that of CD_4 (*SI Appendix*, p. S19 and Table S5) at 865 °C, yielding KIE = 1.78 ± 0.18 and arguing that C–H bond cleavage is involved in the rate-limiting step. This value is similar to OCM KIEs reported over oxide catalysts, which range between 1.2 and 1.8 (39, 54–56).

Reaction Pathways and Networks. Rigorous kinetic analyses are challenging for complex reaction systems with multiple pathways. The Delplot analysis procedure of Bhore et al. (57) plots selectivity or yield for a particular product (y) divided by the reaction conversion (x) vs. conversion and extrapolates the plot back to zero conversion $\left(\lim_{x\to 0}\frac{y}{x}\right)$, enabling primary product determination (those with nonzero positive intercepts) and nonprimary products (those with intercepts approaching zero). A multirank Delplot analysis was carried out to determine the product ranks and to construct an approximate reaction network. Fig. 3 shows the first- (Fig. 3*A*), second- (Fig. 3*B*), and third- (Fig. 3*C*) rank Delplots for SOCM. Note that the sum of all gaseous product selectivities is slightly below 100%, possibly due to minor coke formation (34). The intercepts for C_2H_6, C_2H_4, and CS_2 appear nonzero in the

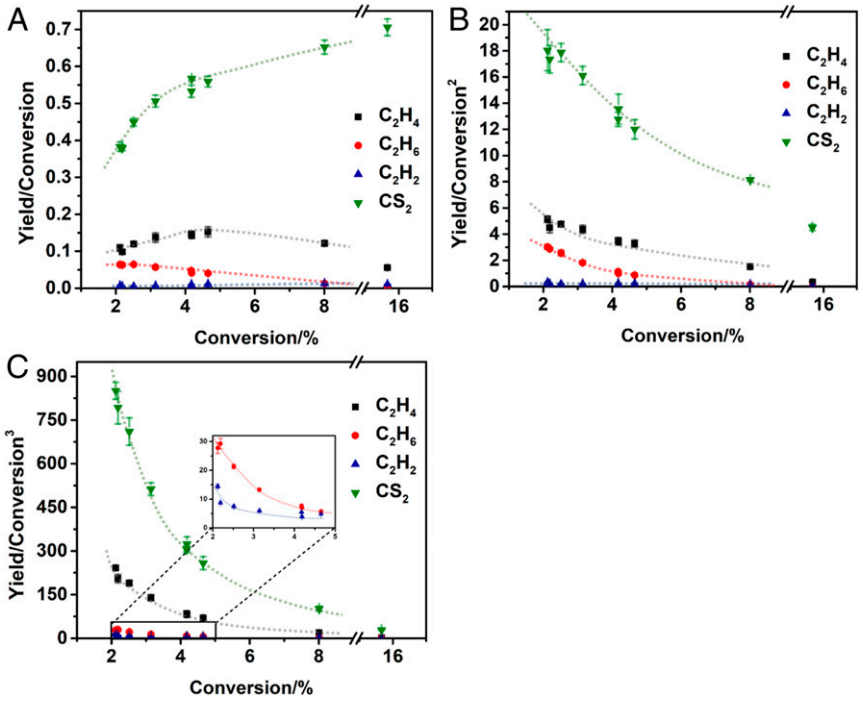

Fig. 3. SOCM Delplots for methane: first-rank Delplot (*A*), second-rank Delplot (*B*), and third-rank Delplot (*C*) for the SOCM reaction over an Fe_3O_4-based catalyst. Reaction condition: 865 °C, CH_4:S_2 = 1.099, WHSV range: 0.13 h^{-1} ~ 0.98 h^{-1}.

first-rank Delplot, while the intercept for C_2H_2 is zero. In the second-rank Delplot, the intercepts of all products diverge except for C_2H_2. In the third-rank Delplot, the intercepts of all products diverge. These results suggest that methane reacts directly to form ethane, ethylene, and carbon disulfide (pathway A), whereas acetylene is a secondary product, not directly formed from methane (pathway B). Similarly, the first- and second-rank Delplots for ethane (*SI Appendix*, Fig. S11) indicate that ethane almost exclusively reacts to form ethylene, while CS_2 is a higher-rank product of ethane. The first-rank ethylene Delplot (*SI Appendix*, Fig. S12*A*) shows that the C_2H_2 is a primary product of ethylene, whereas the first-rank acetylene Delplot (*SI Appendix*, Fig. S13*A*) indicates that acetylene primarily forms CS_2. For acetylene, as conversion falls, the carbon balance strays further from 100%, likely due to coking. Note that a Delplot analysis only provides the shortest route in a reaction network. From the data in Fig. 3 it is likely that methane undergoes a series of C–H activation steps to directly form C_2H_4, C_2H_6, and CS_2, while C_2H_2 is likely formed via C_2H_4 dehydrogenation. However, stepwise dehydrogenation from C_2H_6 to C_2H_4 to C_2H_2 cannot be ruled out and is in agreement with the ethylene and acetylene Delplots. See more below.

SOCM Reaction Sequence. Additional insights into the SOCM reaction sequences follow from hydrocarbon product distributions vs. contact time (t_c). CH_4 experiments were carried out at low conversions, verified by a linear CH_4 conversion vs. t_c relation. SOCM C_2 product yields to C_2H_4 (the major product), C_2H_6, and C_2H_2 (very minor product) vs. t_c (Fig. 4*A*) reveal that C_2H_6 yield peaks early ($t_c \approx 0.1$ s) and rapidly decays, while the C_2H_4 and C_2H_2 yields maximize after $t_c \approx 0.4$ s and $t_c \approx 0.6$ s, respectively. The C_2H_4 yield then decays rapidly, whereas the C_2H_2 yield remains constant for a longer period before decaying. The relative evolution of the C_2H_6, C_2H_4, and C_2H_2 yields with t_c suggests the possible sequence: $CH_4 \rightarrow C_2H_6 \rightarrow C_2H_4 \rightarrow C_2H_2$. Fig. 4*B* plots total C_2 and CS_2 yields vs. t_c. The CS_2 yield increases linearly with increasing t_c from $t_c = 0.07$ s to 0.66 s and then increases more gradually, maximizing at $t_c = 1.33$ s. Note that the C_2 yield does not decay during the initial CS_2 yield rise, but falls during the more gradual CS_2 increase at $t_c > 0.2$ s. This suggests that the major CS_2 fraction at low t_c likely arises from direct $CH_4 \rightarrow CS_2$ conversion, while the increased CS_2 selectivity at $t_c > 0.2$ s may reflect some conversion of C_2 intermediates to CS_2.

To examine the extent that SOCM C_2 products undergo conversion to CS_2, ethane oxidation with S_2 was studied at $C_2/S_2 \approx 1.1$. Note that the relative product concentrations are different from those in SOCM. Ekstrom and Lapszewicz (58) reported that CH_4 OCM conversion is suppressed by addition of C_2 species due to competition for active sites. In SOCM, C_2H_6 conversions are >50% at all weight hourly space velocities (WHSVs). Fig. 4*C* shows the yield to CH_4, C_2H_4, C_2H_2, and CS_2. Note from Fig. 4 *B* and *C* that at similar $t_c = 0.66$ s the CS_2 yield reaches 11% and 5% for methane and ethane, respectively, arguing that $C_2 \rightarrow CS_2$ is slower than $CH_4 \rightarrow CS_2$, in agreement with the Delplot data showing that CS_2 is a first-rank product. The increased CS_2 yield in Fig. 4*C* with a concomitant fall in C_2H_4 yield suggests that $C_2H_4 \rightarrow C_2H_2$ conversion may also reflect a $C_2H_4 \rightarrow CS_2$ process. C_2H_2 oxidation with S_2 was studied at a C_2H_2/S_2 ratio of ≈1.1 (*SI Appendix*, Fig. S13 *A* and *B*). Similar to C_2H_6 oxidation, CS_2 selectivity rises from 30 to 60%, within $t_c = 0.088$ to 0.500 s, correlating with direct $C_2H_2 \rightarrow CS_2$ oxidation.

Discussion of Experimental Results. The surface characterization data indicate that sulfurized Fe_3O_4 consists largely of two phases, FeS and FeS_2, with the latter catalytically most significant, as suggested in *Theoretical Analysis of the SOCM Reaction Mechanism* below. The kinetic data indicate that the rate of methane

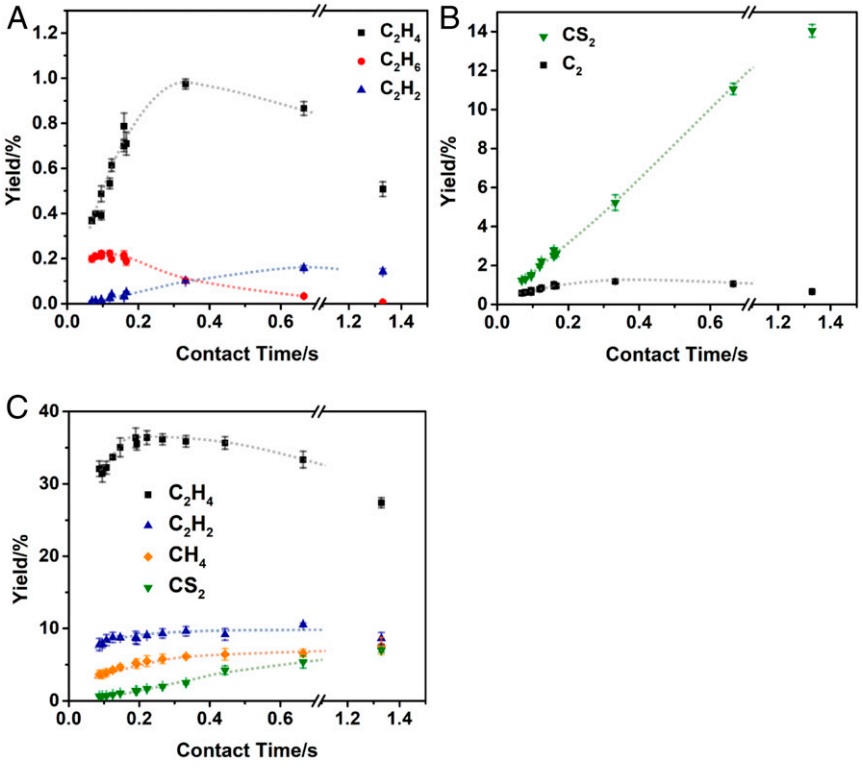

Fig. 4. SOCM product distributions as function of catalyst contact time using methane and ethane as feeds. (*A*) Methane: yield to C_2H_6 (red), C_2H_4 (black), and C_2H_2 (blue), (*B*) Methane: yield to combined C_2 products (black) and CS_2 (green) in SOCM as a function of contact time. (*C*) Ethane: yield toward C_2H_4 (black), C_2H_2 (blue), CH_4 (orange), and CS_2 (green). Reaction condition: 865 °C, WHSV range: 0.13 h^{-1} ~ 0.98 h^{-1}, CH_4:S_2 = 1.099 (*A* and *B*), C_2H_6:S_2 = 1.099 (*C*).

conversion is first-order in both CH_4 and S_2 partial pressures (*SI Appendix*, Fig. S6). The first-order S_2 dependence suggests that surface-bound S_2^* species are the dominant participant in the rate-limiting step and may account for the lower 66 ± 8 kJ/mol activation energy vs. >100 kJ/mol typical for OCM (39, 54, 59, 60). The higher OCM E_{act} may reflect that C–H activation involves only a single O site (here $r_{OCM} = k'_{OCM}K_{O2}^{1/2}P_{O2}^{1/2}$) whereas the apparent activation in SOCM occurs over an S_2^* site ($r_{SOCM} = k'_{SOCM}K_{S2}P_{S2}$) and may also reflect a more energetically demanding dissociative adsorption of O_2 vs. molecular adsorption of S_2 (33). See *Theoretical Analysis of the SOCM Reaction Mechanism* below. Similar analysis shows that the rate of ethylene formation is also first-order in the partial pressures of CH_4 and S_2 (*SI Appendix*, Fig. S7)

As shown in Fig. 3, methane can be directly converted to C_2H_4, C_2H_6, and CS_2. With KIE = 1.78, the rate-determining SOCM step reasonably involves methane C–H cleavage, in accord with the first-order kinetics in methane as well as OCM results (39, 52–54, 59–61). The methane SOCM Delplot extrapolated intercepts of Fig. 3 show that C_2H_4, C_2H_6, and CS_2 are directly formed from methane, with CS_2 formation faster than that of C_2H_4 and C_2H_6. The direct formation of C_2H_4 from methane confirms the occurrence of a primary SOCM pathway involving C–H abstraction from adsorbed CH_3^* to form CH_2^* species and their subsequent coupling. C_2H_4 can also arise from secondary ethane dehydrogenation pathways. C_2H_2, however, does not appear to form directly from methane. That CS_2 is readily formed from methane, while acetylene formation is prohibited, strongly suggests that a CH intermediate, if formed, is more reactive for oxidation than coupling. Furthermore, Delplots (*SI Appendix*, Figs. S11–S13) confirm ethylene dehydrogenation to form acetylene. Fig. 4 shows that SOCM product distribution varies with contact time t_c, with the C_2H_6 yield highest at $t_c \approx 0.15$ s while C_2H_4 and C_2H_2 maximize at $t_c \approx 0.25$ s and ≈ 0.65 s, respectively. This suggests that C_2H_4 and C_2H_2 may also arise, to some extent, via successive C_2H_6 and C_2H_4 dehydrogenation.

The above reaction sequence data indicate that the predominant pathways for ethylene and CS_2 formation are different. CS_2 is primarily formed directly from CH_4, as evident in Fig. 4, where CS_2 yield increases with the C_2 yield at low t_c. In contrast, ethylene likely forms via a primary pathway (evident in the Delplot) as well as a secondary pathway via ethane dehydrogenation. OCM studies by Hutchings et al. (62) over Li/MgO and Lunsford and coworkers (63) over $Mn/Na_2WO_4/SiO_2$ and $Mn/Na_2WO_4/MgO$ reported small amounts of C_2H_4 formed directly from CH_4 at short contact times, but the majority is formed via C_2H_6 dehydrogenation. Furthermore, at 830 °C Baerns and coworkers (64) reported an OCM C_2H_6 yield maximum at shorter t_cs than C_2H_4, again providing evidence for stepwise dehydrogenation. See more in the discussion of the DFT results reported below.

The dehydrogenation pathway is also supported by comparing the relative methane and C_2 reactivities. Fig. 4 shows the 865 °C conversions of CH_4, C_2H_6, C_2H_2, and CS_2 at differing contact times. The CS_2 conversion is zero, the CH_4 conversion is less than that of C_2H_2, while that of C_2H_6 is highest at both contact times. Taking into account that for all t_cs the C_2H_4 yield is greater than that of both C_2H_2 and C_2H_6, and that C_2H_4 yield is always greater than C_2H_6 under the present conditions, we conclude that SOCM hydrocarbon reactivity increases in the order $CH_4 < C_2H_4 < C_2H_2 < C_2H_6$. The greater reactivity of C_2H_6 vs. C_2H_4 implies rapid oxidation of C_2H_6 to C_2H_4. This is reflected in the high C_2H_4/C_2H_6 yield ratio of 9 to 12, typical of other SOCM catalysts (34). Nevertheless, a major C_2H_4 fraction forms directly from CH_4 via coupling of CH_2 intermediates as argued by the Delplots above and DFT analysis below.

Theoretical Analysis of the SOCM Reaction Mechanism. Complementary first-principles DFT calculations were used to probe SOCM elementary reaction pathways, the nature of the active sites, and plausible mechanisms for direct methane conversion to C_2H_6, C_2H_4 and CS_2 over sulfided Fe_3O_4. The above experimental results argue that the path involving subsequent CH_x C–H scission steps is critical in methane activation and in C_2 and CS_2 formation. As such, theory was used to examine the mechanism and sites for CH_4 activation and the formation of the desired C_2H_4 and undesired CS_2 products via this CH_x path. Ab initio thermodynamic simulations were initially carried out to determine the lowest-energy FeS_x surface structures and the nature of the active surface sites under different reaction conditions. The reaction energies and activation barriers for adsorption of S_2 and CH_4 activation and subsequent pathways to C_xH_y and CS_2 products were calculated at 0 K. These electronic energies were used as approximations of the activation enthalpies and used with Arrhenius theory and kinetic models to establish temperature effects, apparent activation barriers, and reaction rate orders. Frequency calculations were carried out to determine the zero-point energy, thermal corrections to energies, and entropies were then used to calculate the free energies of elementary adsorption and reaction and desorption steps. See details in *SI Appendix*.

The above pXRD, XPS, Raman, and SEM/TEM analyses identify FeS as the dominant postsulfurization phase with FeS_2 present as a nanocrystalline and/or surface amorphous layer. The theoretical analyses thus examined both the FeS and FeS_2 phases. DFT ab initio thermodynamic calculations show FeS to be the dominant phase. Surface free-energy analysis for the 001Fe, 010Fe, 0102S, 010S, and 001S surfaces as a function of S_2 pressure indicate that the 001S terminated surface has the lowest energy over a wide pressure range. However, the methane activation barriers on the FeS 001S surface as well as the other FeS surfaces are computed to be >300 kJ/mol, strongly suggesting that the FeS surface and phase are catalytically unimportant (see *SI Appendix*, pp. S47–S51 for details). Similar ab initio analyses by Alfonso (65) for the different surface terminations of the 001, 011, 210, and 111 FeS_2 surfaces as a function of the S chemical potential showed that the 001-S terminated FeS_2 surface is lowest in energy under the relevant S chemical potentials. Overall, the DFT and characterization studies indicate that the S-terminated 001-S FeS_2 surface is

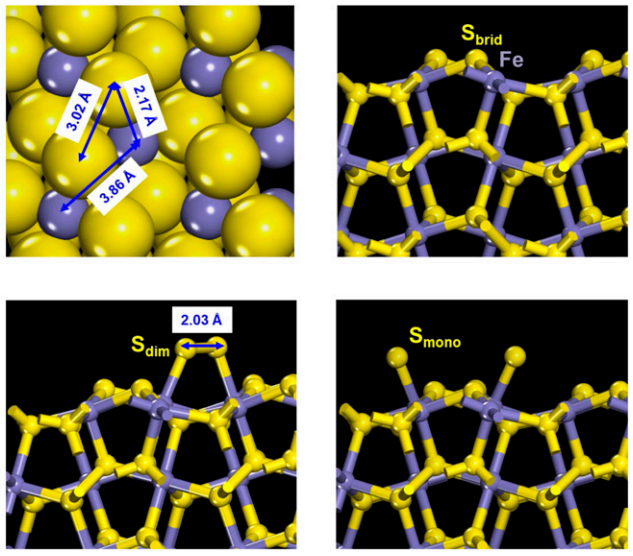

Fig. 5. SOCM active sites on FeS_2 (*A*) Top (*Left*) and side view (*Right*) of the model sulfur terminated-001S FeS_2 surface used to model SOCM over a sulfided Fe_3O_4 catalyst. (*B*) Adsorbed sulfur dimer sites (S_{dim}) (*Left*) and adsorbed monomeric sulfur sites (S_{mono}) (*Right*) formed on the FeS_2 surface. As S_2 is adsorbed over the FeS_2 surface, the S–S bond distance elongates from a gas phase distance of 1.91 Å to 2.03 Å. Sulfur atoms are shown in yellow and iron atoms in purple.

active for methane conversion and hence was used to model the working sulfided Fe_3O_4 surface and to examine the surface chemistry (see *SI Appendix* for surface modeling details).

The sulfur-terminated 001-S FeS_2 surface is composed of exposed Fe and S_{brid} atoms that bridge the Fe surface sites (Fig. 5*A*) and contains S_{brid}–S_{brid}, Fe–S_{brid}, and Fe–Fe site pairs that could all potentially carry out C–H activation. Methane activation was therefore examined at all three site pairs. The transition state for C–H activation over the Fe–Fe site pair could not be isolated, likely reflecting the long 3.86 Å Fe···Fe distance which impedes concerted C–H activation over Fe–Fe site pairs. However, activation barriers of 261 and 163 kJ/mol (ΔG_{act} = 362 and 254 kJ/mol, respectively) were computed for methane C–H activation over the S_{brid}–S_{brid} and Fe–S_{brid} sites, respectively. The lower Fe–S_{brid} pair barrier suggests such sites are favored for initial methane activation over S_{brid}–S_{brid} sites.

In addition to these atomic site pairs, gaseous S_2 can adsorb onto exposed Fe surface sites, yielding chemisorbed S_2*. The two sulfur atoms of bound S_2* can be catalytically active. Similar molecularly adsorbed O_2* species are thought to dissociate to form active O* species in OCM C–H activation (8, 66). Molecular S_2 is found here to adsorb most favorably in a di-σ configuration to two neighboring exposed Fe sites, yielding a strongly bound sulfur dimer (S_{dim} in Fig. 5*B*) with an energy of −215 kJ/mol. S_2* can subsequently dissociate over the two Fe sites to which it is adsorbed to yield monoatomic terminal sulfur site pairs (S_{mono}–S_{mono}; Fig. 5*B*). While direct S_2 dimer activation to form these monomeric species (S_{mono}) is far less exothermic (ΔE_{rxn} = −25 kJ/mol, ΔG_{rxn} = 78 kJ/mol) than S_2 adsorption (ΔE_{ads} = −215 kJ/mol, ΔG_{ads}= −104 kJ/mol), the barrier for methane C–H bond activation is significantly lower at S_{mono} site pairs than over the S_{dim} site, as discussed below. The active catalytic surfaces under SOCM conditions are likely covered with S due to the higher pressures of S_2 used. Exposed metal sites, however, can readily form at the high SOCM CH_4/S_2 ratios (~1.099) and temperatures used, as over PdS (29). As such, Fe–S_{brid}, S_{dim} (S_2*), and S_{mono}–S_{mono} site pairs are all likely present under SOCM conditions and can participate in the surface chemistry.

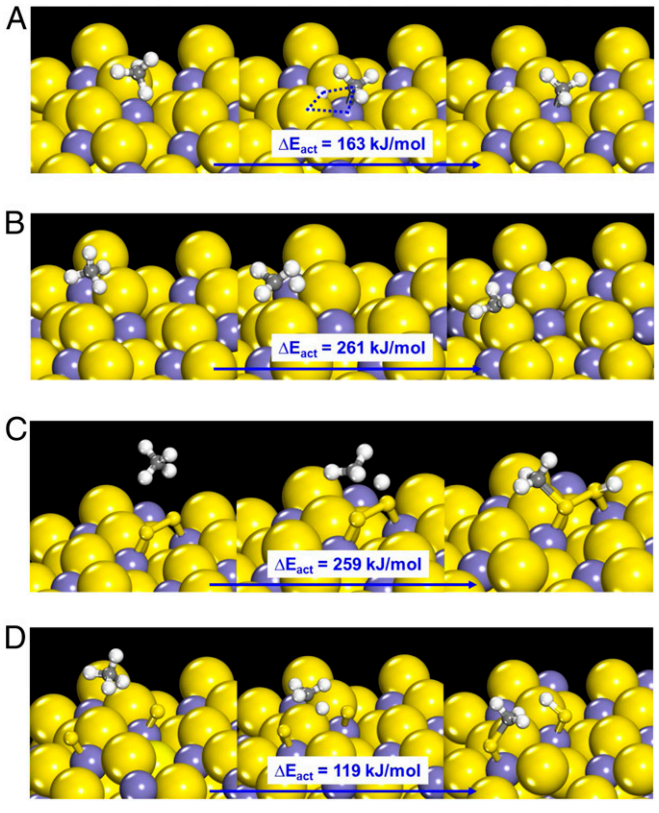

Fig. 6. SOCM methane C–H activation over the surface and adsorbed sites of a sulfided Fe_3O_4 catalyst (FeS_2). Optimized reactant, transition state, and product structures for initial methane C–H bond activation over (*A*) Fe–S_{brid} site pairs, the (*B*) bridged sulfur site pairs (S_{brid}–S_{brid}), (*C*) S_{dim} site, and the (*D*) S_{mono}–S_{mono} site pairs. Methane activation over the Fe–S_{brid} proceeds via a four-centered transition state (shown via dotted blue lines), whereas activation over S_{brid}–S_{brid}, S_{dim}, and S_{mono}–S_{mono} sites proceeds via a radical-like mechanism. Yellow, S; purple, Fe; white, H; gray, C. The reported activation barriers are calculated at 0 K.

Methane activation over the Fe–S_{brid} site pairs proceeds with a computed barrier of 163 kJ/mol (ΔG_{act} = 254 kJ/mol) via C–H bond scission involving Fe atom insertion into the methane C–H bond, together with simultaneous H abstraction by a neighboring S_{brid} site via a four-centered *Fe–C–H–S* transition state (Fig. 6*A*). This ligand-assisted C–H activation is similar to σ-bond metathesis processes (67–69). A Bader charge analysis (70) for this reaction shows an increase of 0.23 e^- on the CH_3 group and a loss of 0.18 e^- on the H atom in proceeding from the initial state to the transition state. This suggests heterolytic C–H activation similar to that found for methane activation over PdS (29), PdO (71), CuO (72), and MgO (52) surfaces. In contrast to the above scenario, methane C–H bond activation over bridging sulfur sites (S_{brid}–S_{brid}) proceeds via a homolytic mechanism with a computed barrier of 261 kJ/mol (ΔG_{act} = 362 kJ/mol) where the CH_3 and H assume free radical character on C–H bond activation (Fig. 6*B*). The transition state for this initial C–H activation involves an H atom that is nearly fully bound to a surface S and a free CH_3 radical which weakly interacts with the surface. Bader TS charge analyses show a gain of 0.07 e^- for the CH_3 group, indicating radical-like character. Similar H-abstraction transition states are reported for O-covered metal surfaces (73), reducible metal oxides (74, 75), and S-covered metal sulfides (29). These results also concur with recent OCM studies on Li-doped MgO which indicate that $\cdot CH_3$ formation only proceeds in the presence of O_2 (52).

Methane activation over the dimeric S_{dim} and terminal monomeric S_{mono}–S_{mono} surface sites which can also be present proceeds via a similar homolytic C–H activation mechanism (Fig. 6 *C* and *D*). The intrinsic electronic energy barriers over the S_{dim} and S_{mono}–S_{mono} sites are computed to be lower than over the S_{brid}–S_{brid} sites (261 kJ/mol), with energies of 259 kJ/mol (ΔG_{act} = 343 kJ/mol) and 119 kJ/mol (ΔG_{act} = 204 kJ/mol), respectively. While the intrinsic C–H activation barrier over the two monomeric S_{mono} sites is significantly lower than over S_{dim} sites, there is a higher energetic cost to activate S_2* (S_{dim}) to form these reactive S_{mono} sites. The higher energy cost thus limits the concentration of S_{mono} sites and in turn limits methane activation at these sites. In contrast, methane activation over S_{dim} sites is preceded by an exothermic adsorption step that lowers the overall apparent barrier and thus makes it equally probable to catalyze methane C–H activation as that over the Fe–S_{brid} sites.

The CH_3* species produced in the above processes can subsequently react to form ethane, ethylene, and/or CS_2, the selectivities of which are governed by competition between C–C coupling and C–H activation rates. C–C coupling to form C_2 products can either occur via surface intermediates or gas-phase radicals generated via desorption of adsorbed CH_x* intermediates from the catalyst surface. As methane is most favorably activated over the Fe–S_{brid} and S_{dim} sites, we examined the subsequent C–H activation, C–C bond formation, and desorption steps for the CH_3*, CH_2*, and CH* intermediates adsorbed on the S_{dim} and Fe–S_{brid} site pairs to probe product selectivities. The results in Table 1 show that the free energy barriers for CH_x* intermediate C–H activation are lower than the barriers for C–C coupling and desorption from the S_{dim} sites. As such, the resulting CH_x* intermediates formed on these surface

Table 1. Computed SOCM C–H activation, C–C coupling free energy barriers, and desorption free energies over the Fe–S_{brid} and S_{dim} catalytic sites of the FeS_2 surface

	C–H activation free energy barrier, kJ/mol		C–C coupling free energy barrier, kJ/mol		Desorption free energies, kJ/mol	
Species	Fe–S_{brid} site	S_{dim} site	Fe–S_{brid} site	S_{dim} site	Fe–S_{brid} site	S_{dim} site
CH_3	189	115	209	285	81	127
CH_2	188	26	48	64	234	292
CH	189	175	83	412	321	558

sulfur sites preferentially undergo subsequent C–H activation. Thus, methane would preferentially fully oxidize at these sites to form CS_2 via C–H activation, suggesting that while the adsorbed S_{dim} sites readily activate methane they also catalyze direct CS_2 formation as a primary product; similar results hold for S_{mono}–S_{mono} site pairs (*SI Appendix*, Table S7). This scenario interestingly parallels the role of adsorbed O species thought responsible for methane overoxidation to CO_2 in OCM (8) and agrees with the present experimental data showing that CS_2 is produced as a primary product from CH_4. Note, however, the following: 1) While the free energy barrier for CH_3* intermediate desorption (127 kJ/mol) is greater than that for further activation to form CH_2* (115 kJ/mol), the difference is only 12 kJ/mol. As such, a significant fraction (~20%) of CH_3* intermediates on S_{dim} sites can also desorb as methyl radicals, that can then couple in the gas phase to form ethane. 2) While the free energy barrier for CH_2* (64 kJ/mol) coupling is 18 kJ/mol higher than for C–H activation of CH_2* (26 kJ/mol shown in Table 1), it can similarly be argued that CH_2* coupling over these adsorbed sulfur sites to form ethylene can still proceed but to a lower extent than C–H activation of CH_2* to form CS_2, thus explaining the first-order Delplot for ethylene formation (Fig. 3).

A similar analysis for Fe–S_{brid} sites comparing the free energy barrier for CH_3* C–H activation (*SI Appendix*, Fig. S14*A*) to that for desorption, in contrast, shows a large free energy difference of 108 kJ/mol, thus indicating that CH_3 desorption is significantly favored over subsequent C–H bond activation at the Fe sites. Hence, over the Fe–S_{brid} sites there is exclusive formation of methyl radicals, which can couple in the gas phase to form ethane as in OCM (5, 76–78). Ethane can then undergo facile dehydrogenation to ethylene as discussed above, contributing to the high SOCM ethylene selectivity.

The present SOCM results reveal that methane can be activated over dimeric and monomeric adsorbed sulfur site pairs to primarily form CS_2 and significant quantities of ethylene/ethane. Also, methane is activated over Fe–S_{brid} site pairs to yield ethane as a primary product, which can readily dehydrogenate to form ethylene. Thus, from the different identified active sites, we can write an overall rate expression for methane conversion as the sum of methane activation rates over these sites (Eq. **1**), where L_1 and L_2 correspond to the total concentration of Fe and S_{brid} sites, respectively, and z is the coordination number

$$r = k_{C-H\_FeS}[CH_4][Fe][S_{brid}]\frac{z}{(L_1+L_2)} + k_{C-H\_Sdim}[CH_4][S_{dim}] + k_{C-H\_Smono}[CH_4][S_{mono}]^2\frac{z}{2L_1} \quad [1]$$

of the respective site with the z/L ratios corresponding to the probability of finding the two sites adjacent to one another. Here k_{C-H_FeS}, k_{C-H_Sdim}, and k_{C-H_Smono} refer to the rate constants for C–H bond activation of methane over the Fe–S_{brid}, S_{dim}, and S_{mono}–S_{mono} sites, respectively. Eq. **1** can be simplified by noting the experimental results in Fig. 4*B* that reveal that >50% of the reacted methane is converted directly to CS_2 via a primary pathway. As such, the measured activation barriers can be approximated as those for methane activation over the S_{dim} or S_{mono} sites to form CS_2, yielding Eq. **2**:

$$r = k_{C-H\_Sdim}[CH_4][S_{dim}] + k_{C-H\_Smono}[CH_4][S_{mono}]^2\frac{z}{2L_1}. \quad [2]$$

The experimental SOCM barrier of 66 kJ/mol over FeS_2 reported herein is significantly lower than reported OCM barriers (39, 59, 60). The DFT-computed intrinsic activation barriers along with the heats of molecular and dissociative adsorption presented in *SI Appendix* yield apparent activation barriers, $\Delta E_{app,}$ over the S_{dim} + S_{mono} sites of 44 and 94 kJ/mol, respectively. Using a Boltzmann weighting scheme, we calculate an apparent barrier of 51 kJ/mol over the S_{dim} and S_{mono} sites—15 kJ/mol lower than the overall apparent experimental barrier of 66 ± 8 kJ/mol. Note, however, for simplicity the computed apparent activation barriers were derived by approximating the rate expression only in terms of methane activation over S_{dim} sites that lead to CS_2.

For a more accurate description of the apparent methane activation barrier, and to determine the apparent barriers for C_2 products and CS_2 formation and establish the rate dependencies on methane and S_2, we used the DFT-calculated barriers and entropies for all elementary steps over the Fe–S_{brid}, S_{dim}, and S_{mono} pairs (*SI Appendix*, Fig. S30 and Table S9) to develop a microkinetic model. The rate constants used in the simulations were calculated from the free energies of activation (ΔG_{act}) and

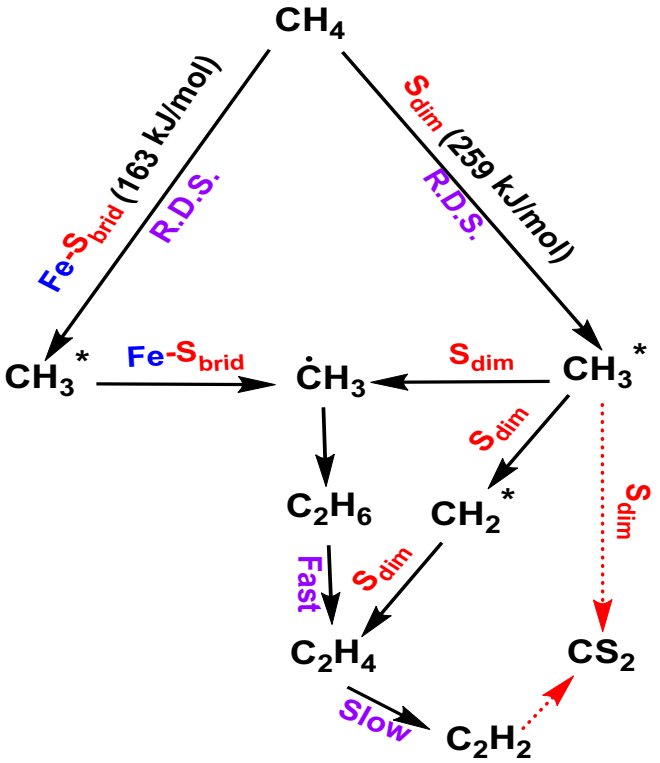

Fig. 7. SOCM overall reaction scheme, summarizing the pathways for CH_4 + S_2 reactions at 865 °C. CH_4 is activated predominantly over S_{dim} or Fe–S sites, with radical recombination, surface coupling, and dehydrogenation yielding C_2 products. CS_2 is largely formed directly from CH_4. The numbers in the brackets correspond to the activation energies (in kilojoules per mole) for methane activation (with respect to gas-phase methane) over the respective sites. R.D.S., rate determining step.

the free energies of reaction (ΔG_{rxn}) for each elementary adsorption, surface reaction, and desorption step as discussed in *SI Appendix*.

Microkinetic simulations were carried over a range of temperatures and pressures to determine the apparent activation barriers and rate dependencies. The overall apparent barrier for methane activation was calculated to be 57 kJ/mol, in good agreement with the measured 66 kJ/mol barrier. The overall barriers for ethylene and CS_2 formation from microkinetic simulations were calculated to be 120 kJ/mol and 23 kJ/mol, respectively, which are higher and lower (but near the DFT uncertainty limits) than the experimental barriers of 85 and 39 kJ/mol, respectively (see *SI Appendix*, p. S34 for more information). Note that the present simulations used all calculated energies and estimated entropies without fitting to experiment. In addition to barriers, the microkinetic model reveals rate orders of 0.89 and 1.0 with respect to the CH_4 and S_2 partial pressures, in close agreement with experiment.

The SOCM pathways established here are shown in Fig. 7. For detailed energetics of the reaction pathways over Fe–S_{brid}, S_{dim}, and S_{mono} sites see *SI Appendix*, Fig. S30. Methane is activated heterolytically over the Fe–S_{brid} site pairs and homolytically over adsorbed sulfur sites (primarily S_{dim}). The resulting CH_3* surface species then react via two parallel pathways to yield C_1 intermediates that ultimately form CS_2 or C_2 intermediates and products. The CH_3* intermediates can desorb to form methyl radicals that subsequently couple in the gas phase to form C_2H_6 that can further dehydrogenate to form C_2H_4, C_2H_2, and finally CS_2. The CH_3* intermediates can also undergo C–H activation to form CH_2*, CH*, C*, or CS_2 over the adsorbed sulfur sites. C_2H_4 also forms via the coupling of CH_2* intermediates over S_{dim} sites. The relative rate for each process is labeled fast or slow in Fig. 7. At short contact times, the low selectivity to the C_2 products vs. that for CS_2 shows that the C_2 product formation rate is slow vs. CS_2 formation. The high C_2H_4 selectivity in the C_2H_6 conversion experiments and the lower C_2H_2 selectivity indicate that C_2H_6 dehydrogenation to C_2H_4 is significantly faster than C_2H_4-to-C_2H_2 dehydrogenation. Finally, the gradual increase in CS_2 yield with increasing contact time for C_2H_6 and C_2H_2 oxidation shows that CS_2 formation rates from the C_2 hydrocarbons are relatively slow.

Comparison of SOCM with Conventional OCM. As noted above, a first-order SOCM rate dependence is observed with respect to both the methane and S_2 partial pressures. This dependence on CH_4 is not unexpected since the first C–H bond activation is rate-limiting, and OCM is similar with a similar KIE (39, 61). However, the present first-order dependence on S_2 partial pressure is noteworthy since most OCM studies report half-order dependence on O_2, where rapid O_2 dissociation and subsequent CH_4 activation by chemisorbed O* or lattice O^-/O^{-2} sites are generally proposed, with the exact nature of active sites still debated (35, 52). Recent investigations by Kwapien et al. (52), however, indicate that the O^{-2} sites are the active sites for methane activation over Li–MgO rather than the O^- sites originally proposed (35).

The apparent SOCM activation energy, 66 kJ/mol, is significantly lower than OCM barriers ranging from 113 to 172 kJ/mol over doped lanthanide and alkaline earth oxides (59, 60) to ≥ 200 kJ/mol over Mn/Na_2WO_4 and other catalysts (39, 59). A good portion of the barrier differences likely reflect differences in what is actually measured. For the Fe–S SOCM system examined here the apparent rate constant is proportional to $k_{C-H}K_{S2}$ (discussed above), while in OCM systems where the rate is half-order in O_2 the apparent rate constant is likely proportional to $k_{C-H}K_{O2}^{1/2}$. The lower apparent activation energy for CS_2 formation suggests that it is kinetically somewhat more favorable than ethylene. In contrast, the overoxidation in OCM to CO_2 is largely attributed to C_2 oxidation (63, 79). OCM kinetic studies for several catalysts show that the CO_x formation rate for the oxidative conversion of C_2H_4 or C_2H_6 is up to 6.5 times greater than that for the direct oxidation of CH_4 (79). As such, the intercept for CO_2 formation is zero in a first-rank Delplot for methane OCM over 16% Li/TiO_2, 9% $Li/NiTiO_3$, and 17% Li/La_2O_3 catalysts (59), whereas a nonzero intercept is observed here for CS_2. The different Delplot ranks of CO_2 and CS_2, as well as the rate laws, clearly indicate that the SOCM mechanism is significantly different from that of OCM, with the overoxidation products formed predominantly via different pathways. Furthermore, the OCM literature describes nonzero intercepts for C_2H_6 and C_2H_4 in first-rank Delplots over the aforementioned catalysts (59). Similar nonzero SOCM intercepts are seen in Fig. 3*A*, which can be partially attributed to the relatively rapid rate of activating the weaker ethane C–H bond vs. the stronger methane C–H bond in addition to direct ethylene formation via CH_2* coupling (33).

The present C_2 selectivity contrasts with OCM, where nearly all reported C_2H_4/C_2H_6 product ratios are <<1 (17, 37, 59, 80–82). Considering the lower C–H bond dissociation energy of C_2H_6 (420 kJ/mol) vs. C_2H_4 (463 kJ/mol) (83), a higher reactivity of C_2H_6 over C_2H_4 is, all other things being equal, expected for both OCM and SOCM. Note, however, that gas-phase reactivity data indicate that hydrocarbon C–H bond cleavage also depends on the H affinity of the H abstractant (84, 85). Previous OCM studies showed that the relative activation energies for C_2H_6 and C_2H_4 strongly depend on the activating species (*SI Appendix*, Table S6) (86). Thus, surface OCM O* species are likely to have different relative activation energies and yield different product distributions than surface SOCM S_2* species, plausibly yielding higher SOCM C_2H_4/C_2H_6 ratios. Also, the direct formation of ethylene via coupling of CH_2* intermediates observed here can in addition account for the higher C_2H_4/C_2H_6 ratios. In OCM, the selectivity to acetylene is usually negligible (87) since any acetylene formed is immediately oxidized to CO_2 over oxide surfaces (88). In contrast, acetylene readily forms in the present SOCM and is more stable because the thermodynamically weaker S_2 oxidizing power vs. O_2, limiting acetylene overoxidation and affording selectivity of 2%. Note also an OCM study by Takanabe and Iglesia (89), where added H_2O generates ·OH radicals which enhance rate and selectivity. While SOCM studies of whether analogous ·SH radicals similarly impact the reaction rate and C_2 yield have not been conducted, the zero-order dependence on H_2S concentration does not currently favor such a picture.

Conclusions

S_2 vapor serves as a "soft" oxidant in the catalytic conversion of methane to C_2 products over sulfided Fe_3O_4 with selectivities as high as 33% (34). Kinetic/mechanistic analysis of SOCM shows that ethylene and ethane both are produced as primary products of methane activation. DFT analysis argues that ethane is formed via coupling of gas phase methyl radicals formed via desorption of methyl intermediates from the Fe–S_{brid} and S_{dim} sites. Primary ethylene, on the other hand, is formed via coupling of CH_2 intermediates over the adsorbed sulfur sites (primarily S_{dim}) on the heavily sulfided Fe_3O_4 surface. C_2H_4 yields are limited by competing direct CH_4 to CS_2 conversion and by C_2H_4 overoxidation. These C–H activation processes appear to proceed over the adsorbed sulfur sites which are highly active for C–H cleavage. This is different from OCM, where CO_x is predominantly formed via C_2 product oxidation. In addition to primary ethylene product formation, rapid dehydrogenation of C_2H_6 vs. C_2H_4 yields C_2H_4/C_2H_6 ratios >>1 in SOCM, while typical OCM processes yield ratios of <<1. In contrast to OCM kinetic studies, which typically report half-order in O_2 methane conversion rates, the SOCM reaction order is first-order in S_2. First-order behavior is consistent with involvement of two sulfur sites in the rate-determining methane C–H activation over the adsorbed S_2* sites (S_{dim}). A summary of reaction pathways over Fe–S, S_{dim}, and S_{mono} sites is provided in *SI Appendix*, Fig. S30. The experimental apparent activation energy for SOCM of 66 ± 8 kJ/mol is significantly lower than the 109

Table 2. Comparison of OCM vs. SOCM mechanism and catalytic performance with references

	OCM	SOCM (this work)
Conversion/selectivity	CH_4 conversions: 40–50% C_2 selectivities: 60–70% (35, 36, 59, 90)	CH_4 conversions: 7–10% C_2 selectivities: 20–37% (34)
C_2H_4/C_2H_6 product ratio	Usually smaller than 1 (37, 59)	9–12 (34)
Catalyst stability	Poor for many catalysts (38, 59, 90)	Negligible deactivation observed (34)
Overoxidation	CO_2 formed via C_2 product oxidation (63, 79)	CS_2 formed directly from CH_4
Apparent E_a	113–200 kJ/mol (39, 59)	66 ± 8 kJ/mol
C_2H_2 formation	Not observed or not detectable (87)	1–2%
Rate law	Rate ~ $[CH_4]^1$ $[O_2]^{1/2}$ (39, 63, 64)	Rate ~ $[CH_4]^1$ $[S_2]^1$
KIE (CD_4/CH_4)	Mostly 1.2–1.61, 1.8 over CeO_2 (39, 55, 56, 61)	1.78 ± 0.18

to 259 kJ/mol reported in OCM studies. DFT results indicate that the lower barrier reflects the strong heat of adsorption of sulfur on the surface, significantly lowering the apparent activation energy. A detailed comparison of SOCM vs. OCM phenomenology is presented in Table 2. These insights should help guide the future design of more active and selective direct methane to ethylene conversion processes.

Materials and Methods

Detailed information on materials and methods used is provided in *SI Appendix*, including catalyst preparation and characterization, kinetic and kinetic isotope measurements, Delplots, activation energies, computational analysis of catalytic bond-breaking and coupling processes, thermodynamics of the catalyst surface structure, computed rate law and activation energies, and a summary of reaction pathways over the various catalyst surfaces.

Data Availability. All study data are included in the article and/or *SI Appendix*.

ACKNOWLEDGMENTS. We thank the Center for Innovative and Strategic Transformation of Alkane Resources (NSF Award EEC-1647722) for funding. We also thank the Minnesota Supercomputing Institute at the University of Minnesota and the Pacific Northwest National Laboratory for computing resources. We thank Profs. F. H. Ribeiro, P. C. Stair, J. M. Notestein, and H. H. Kung and Dr. N. Schweitzer for helpful discussions. The work made use of the Electron Probe Instrumentation Center facility of Northwestern University Atomic and Nanoscale Characterization Experimental Center (NU*ANCE*), which received support from the Materials Research Science and Engineering Center program (NSF Grant DMR-1720139) and the Soft and Hybrid Nanotechnology Experimental (SHyNE) Resource (NSF Grant ECCS-1542205) at the Northwestern University Materials Research Center. We thank Dr. D. Wang and Prof. E. Weitz for assisting with the Raman spectra, and M.P. thanks the German Research Foundation (DFG) for a postdoctoral fellowship.

1. R. Horn, R. Schlögl, Methane activation by heterogeneous catalysis. *Catal. Lett.* **145**, 23–39 (2015).
2. X. Guo *et al.*, Direct, nonoxidative conversion of methane to ethylene, aromatics, and hydrogen. *Science* **344**, 616–619 (2014).
3. A. Alshammari, D. V. N. Kalevaru, A. Bagabas, A. Martin, "Production of ethylene and its commercial importance in the global market" in *Petrochemical Catalyst Materials, Processes, and Emerging Technologies*, H. Al-Megren, T. Xiao, Eds. (IGI Global, 2016), pp. 82–115.
4. T. Ito, J. X. Wang, C. H. Lin, J. H. Lunsford, Oxidative dimerization of methane over a lithium-promoted magnesium oxide catalyst. *J. Am. Chem. Soc.* **107**, 5062–5068 (1985).
5. K. D. Campbell, E. Morales, J. H. Lunsford, Gas-phase coupling of methyl radicals during the catalytic partial oxidation of methane. *J. Am. Chem. Soc.* **109**, 7900–7901 (1987).
6. J. S. Lee, S. T. Oyamat, Oxidative coupling of methane to higher hydrocarbons. *Catal. Rev.* **30**, 249–280 (1988).
7. W. Weng, M. Chen, H. Wan, Y. Liao, High-temperature in situ FTIR spectroscopy study of LaOF and BaF_2/LaOF catalysts for methane oxidative coupling. *Catal. Lett.* **53**, 43–50 (1998).
8. E. Mallens, J. H. B. J. Hoebink, G. Marin, An investigation of the oxygen pathways in the oxidative coupling of methane over MgO-based catalysts. *J. Catal.* **160**, 222–234 (1996).
9. P. Myrach *et al.*, Temperature-dependent morphology, magnetic and optical properties of Li-doped MgO. *ChemCatChem* **2**, 854–862 (2010).
10. M. Yildiz *et al.*, Support material variation for the MnxOy-Na_2WO_4/SiO_2 catalyst. *Catal. Today* **228**, 5–14 (2014).
11. K. P. Peil, J. G. Goodwin, G. Marcelin, Surface concentrations and residence times of intermediates on Sm_2O_3 during the oxidative coupling of methane. *J. Am. Chem. Soc.* **112**, 6129–6130 (1990).
12. J. Li *et al.*, Electronic origins of the variable efficiency of room-temperature methane activation by homo- and heteronuclear cluster oxide cations [XYO2](+) (X, Y = Al, Si, Mg): Competition between proton-coupled electron transfer and hydrogen-atom transfer. *J. Am. Chem. Soc.* **138**, 7973–7981 (2016).
13. S. Zhou, J. Li, M. Schlangen, H. Schwarz, Thermal activation of methane by $[HfO]^{(+)}$ and $[XHfO]^{(+)}$ (X=F, Cl, Br, I) and the origin of a remarkable ligand effect. *Angew. Chem. Int. Ed. Engl.* **55**, 7685–7688 (2016).
14. J. Li, S. Zhou, M. Schlangen, T. Weiske, H. Schwarz, Hidden hydride transfer as a decisive mechanistic step in the reactions of the unligated gold carbide $[AuC]^+$ with methane under ambient conditions. *Angew. Chem. Int. Ed. Engl.* **55**, 13072–13075 (2016).
15. J. Li *et al.*, Mechanistic variants in gas-phase metal-oxide mediated activation of methane at ambient conditions. *J. Am. Chem. Soc.* **138**, 11368–11377 (2016).
16. S. Zhou, J. Li, M. Firouzbakht, M. Schlangen, H. Schwarz, Sequential gas-phase activation of carbon dioxide and methane by $[Re(CO)_2]^+$: The sequence of events matters! *J. Am. Chem. Soc.* **139**, 6169–6176 (2017).
17. B. Beck *et al.*, Oxidative coupling of methane–A complex surface/gas phase mechanism with strong impact on the reaction engineering. *Catal. Today* **228**, 212–218 (2014).
18. S. Parishan, P. Littlewood, A. Arinchtein, V. Fleischer, R. Schomäcker, Chemical looping as a reactor concept for the oxidative coupling of methane over the Mn_xO_y–Na_2WO_4/SiO_2 catalyst, benefits and limitation. *Catal. Today* **311**, 40–47 (2018).
19. C. Karakaya, H. Zhu, C. Loebick, J. G. Weissman, R. J. Kee, A detailed reaction mechanism for oxidative coupling of methane over Mn/Na2WO4/SiO2 catalyst for non-isothermal conditions. *Catal. Today* **312**, 10–22 (2018).
20. G. E. Keller, M. M. Bhasin, Synthesis of ethylene via oxidative coupling of methane I. Determination of active catalysts. *J. Catal.* **73**, 9–19 (1982).
21. S. Hamakawa, T. Hibino, H. Iwahara, Electrochemical methane coupling using protonic conductors. *J. Electrochem. Soc.* **140**, 459–462 (1993).
22. J. Langguth, R. Dittmeyer, H. Hofmann, G. Tomandl, Studies on oxidative coupling of methane using high-temperature proton-conducting membranes. *Appl. Catal. Gen.* **158**, 287–305 (1997).
23. L. Chen, L. Lin, Z. Xu, T. Zhang, X. Li, Promotional effect of Pt on non-oxidative methane transformation over Mo-HZSM-5 catalyst. *Catal. Lett.* **39**, 169–172 (1996).
24. J. Zhang, Y. Yang, J. Zhang, Q. Liu, K. Tan, Non-oxidative coupling of methane to C_2 hydrocarbons under above-atmospheric pressure using pulsed microwave plasma. *Energy Fuels* **16**, 687–693 (2002).
25. M. S. Khan, B. L. Crynes, Survey of recent methane pyrolysis literature. *Ind. Eng. Chem.* **62**, 54–59 (1970).
26. H. Jiang, Z. Cao, S. Schirrmeister, T. Schiestel, J. Caro, A coupling strategy to produce hydrogen and ethylene in a membrane reactor. *Angew. Chem. Int. Ed. Engl.* **49**, 5656–5660 (2010).
27. H. Sheng, E. P. Schreiner, W. Zheng, R. F. Lobo, Non-oxidative coupling of methane to ethylene using Mo_2 C/[B]ZSM-5. *ChemPhysChem* **19**, 504–511 (2018).
28. Y. Xiao, A. Varma, Highly selective nonoxidative coupling of methane over Pt-Bi bimetallic catalysts. *ACS Catal.* **8**, 2735–2740 (2018).
29. Q. Zhu *et al.*, Sulfur as a selective 'soft' oxidant for catalytic methane conversion probed by experiment and theory. *Nat. Chem.* **5**, 104–109 (2013).
30. B. Meyer, Elemental sulfur. *Chem. Rev.* **76**, 367–388 (1976).
31. H. Rau, T. R. N. Kutty, J. R. F. Guedes de Carvalho, Thermodynamics of sulphur vapour. *J. Chem. Thermodyn.* **5**, 833–844 (1973).
32. A. J. Jackson, D. Tiana, A. Walsh, A universal chemical potential for sulfur vapours. *Chem. Sci.* **7**, 1082–1092 (2016).
33. C. West, D. R. Lide, Eds., *Standard Thermodynamic Properties of Chemical Substances* (CRC Handbook of Chemistry and Physics, CRC Press, 2012), vol. 13, pp. 5.4–5.41.
34. M. Peter, T. J. Marks, Platinum metal-free catalysts for selective soft oxidative methane → ethylene coupling. Scope and mechanistic observations. *J. Am. Chem. Soc.* **137**, 15234–15240 (2015).
35. J. H. Lunsford, The catalytic oxidative coupling of methane. *Angew. Chem. Int. Ed. Engl.* **34**, 970–980 (1995).
36. U. Zavyalova, M. Holena, R. Schlögl, M. Baerns, Statistical analysis of past catalytic data on oxidative methane coupling for new insights into the composition of high-performance catalysts. *ChemCatChem* **3**, 1935–1947 (2011).

37. U. Simon *et al*., Contributions of phase composition and defect structure to the long term stability of Li/MgO catalysts. *Int. J. Mater. Res.* **103**, 1488–1498 (2012).
38. S. Arndt *et al*., A critical assessment of Li/MgO-based catalysts for the oxidative coupling of methane. *Catal. Rev. Sci. Eng.* **53**, 424–514 (2011).
39. K. Takanabe, E. Iglesia, Mechanistic aspects and reaction pathways for oxidative coupling of methane on $Mn/Na_2WO_4/SiO_2$ catalysts. *J. Phys. Chem. C* **113**, 10131–10145 (2009).
40. L. Li, R. W. Borry, E. Iglesia, Design and optimization of catalysts and membrane reactors for the non-oxidative conversion of methane. *Chem. Eng. Sci.* **57**, 4595–4604 (2002).
41. S. Liu, A. M. Arinaga, M. Peter, T. L. Lohr, T. J. Marks, High ethylene yield oxidative dehydrogenation of ethane using sulfur vapor as a soft oxidant. *ChemCatChem* **12**, 4538–4542 (2020).
42. A. M. Arinaga, S. Liu, T. J. Marks, Oxidative dehydrogenation of propane to propene over transition metal sulfides using sulfur as an alternative oxidant. *Catal. Sci. Technol.* **10**, 6840–66848 (2020).
43. J. Z. Jiang *et al*., Mechanochemical synthesis of Fe-S materials. *J. Solid State Chem.* **138**, 114–125 (1998).
44. N. Stojilovic, D. E. Isaacs, Inquiry-based experiment with powder XRD and FeS_2 crystal: "Discovering" the (400) Peak. *J. Chem. Educ.* **96**, 1449–1452 (2019).
45. D. Brion, Etude par spectroscopie de photoelectrons de la degradation superficielle de FeS_2, $CuFeS_2$, ZnS et PbS a l'air et dans l'eau. *Appl. Surf.* **5**, 133–152 (1980).
46. J. C. Carver, G. K. Schweitzer, T. A. Carlson, Use of X-ray photoelectron spectroscopy to study bonding in Cr, Mn, Fe, and Co compounds. *J. Chem. Phys.* **57**, 982–990 (1972).
47. A. Baum *et al*., Phonon anomalies in FeS. *Phys. Rev. B* **97**, 1–11 (2018).
48. H. Vogt, T. Chattopadhyay, H. J. Stolz, Complete first-order Raman spectra of the pyrite structure compounds FeS_2, MnS_2 and SiP_2. *J. Phys. Chem. Solids* **44**, 869–873 (1983).
49. I. Campbell, P. M. Fauchet, The effects of microcrystal size and shape on the one phonon Raman spectra of crystalline semiconductors. *Solid State Commun.* **58**, 739–741 (1986).
50. Y. Gao, X. Zhao, P. Yin, F. Gao, Size-dependent Raman shifts for nanocrystals. *Sci. Rep.* **6**, 20539 (2016).
51. M. Kitajima, Defects in crystals studied by Raman scattering. *Crit. Rev. Solid State Mater. Sci.* **22**, 275–349 (1997).
52. K. Kwapien *et al*., Sites for methane activation on lithium-doped magnesium oxide surfaces. *Angew. Chem. Int. Ed. Engl.* **53**, 8774–8778 (2014).
53. J. Hagen, *Industrial Catalysis: A Practical Approach* (Wiley, 2006).
54. N. W. Cant, C. A. Lukey, P. F. Nelson, R. J. Tyler, The rate controlling step in the oxidative coupling of methane over a lithium-promoted magnesium oxide catalyst. *J. Chem. Soc. Chem. Commun.* , 766–768 (1988).
55. R. Burch, S. C. Tsang, C. Mirodatos, J. G. Sanchez, Kinetic isotope effects in methane coupling on a reducible oxide catalyst. *Catal. Lett.* **7**, 423–430 (1990).
56. P. F. Nelson, C. A. Lukey, N. W. Cant, Measurements of kinetic isotope effects and hydrogen/deuterium distributions over methane oxidative coupling catalysts. *J. Catal.* **120**, 216–230 (1989).
57. N. A. Bhore, M. T. Klein, K. B. Bischoff, The delplot technique: A new method for reaction pathway analysis. *Ind. Eng. Chem. Res.* **29**, 313–316 (1990).
58. A. Ekstrom, J. A. Lapszewicz, A study of the mechanism of the partial oxidation of methane over rare earth oxide catalysts using isotope transient techniques. *Phys. Chem* **93**, 5230–5237 (1989).
59. E. E. Wolf, *Methane Conversion by Oxidative Processes* (Springer, New York, 1992).
60. E. E. Gulcicek, S. D. Colson, L. D. Pfefferle, Multiphoton ionization detection of methyl radicals from catalytic oxidation of methane. *J. Phys. Chem.* **94**, 7069–7074 (1990).
61. N. W. Cant, E. M. Kennedy, P. F. Nelson, Magnitude and origin of the deuterium kinetic isotope effect during methane coupling and related reactions over lithium/magnesium oxide catalysts. *J. Phys. Chem.* **97**, 1445–1450 (1993).
62. G. J. Hutchings, M. S. Scurrell, J. R. Woodhouse, Oxidative coupling of methane using oxide catalysts. *Chem. Soc. Rev.* **18**, 251–283 (1989).
63. S. Pak, P. Qiu, J. H. Lunsford, Elementary reactions in the oxidative coupling of methane over $Mn/Na_2WO_4/SiO_2$ and $Mn/Na_2WO_4/MgO$ catalysts. *J. Catal.* **179**, 222–230 (1998).
64. Z. Stansch, L. Mleczko, M. Baerns, Comprehensive kinetics of oxidative coupling of methane over the La_2O_3/CaO catalyst. *Ind. Eng. Chem. Res.* **36**, 2568–2579 (1997).
65. D. R. Alfonso, Computational investigation of FeS_2 surfaces and prediction of effects of sulfur environment on stabilities. *J. Phys. Chem. C* **114**, 8971–8980 (2010).
66. M. S. Palmer, M. Neurock, M. M. Olken, Periodic density functional theory study of the dissociative adsorption of molecular oxygen over La_2O_3. *J. Phys. Chem. B* **106**, 6543–6547 (2002).
67. C. C. Cummins, S. M. Baxter, P. T. Wolczanski, Methane and benzene activation via transient $(t\text{-}Bu_3SiNH)_2Zr{=}NSi\text{-}t\text{-}Bu_3$. *J. Am. Chem. Soc.* **110**, 8731–8733 (1988).
68. C. C. Cummins *et al*., (Tri-Tert-Butylsilyl)Imido complexes of titanium: Benzene C-H activation and structure of $[(^tBu_3SiNH)Ti]_2(Mu\text{-}NSi^tBu_3)_2$. *J. Am. Chem. Soc.* **113**, 2985–2994 (1991).
69. T. R. Cundari, T. V. Grimes, T. B. Gunnoe, Activation of carbon-hydrogen bonds via 1,2-addition across M-X (X = OH or $NH_(_2)$) bonds of $d(^6)$ transition metals as a potential key step in hydrocarbon functionalization: A computational study. *J. Am. Chem. Soc.* **129**, 13172–13182 (2007).
70. G. Henkelman, A. Arnaldsson, H. Jónsson, A fast and robust algorithm for Bader decomposition of charge density. *Comput. Mater. Sci.* **36**, 354–360 (2006).
71. Y. H. Chin, C. Buda, M. Neurock, E. Iglesia, Consequences of metal-oxide interconversion for C-H bond activation during CH_4 reactions on Pd catalysts. *J. Am. Chem. Soc.* **129**, 15425–15442 (2013).
72. J. J. Varghese, Q. T. Trinh, S. H. Mushrif, Insights into the synergistic role of metal–lattice oxygen site pairs in four-centered C–H bond activation of methane: The case of CuO. *Catal. Sci. Technol.* **6**, 3984–3996 (2016).
73. Y. H. Chin, C. Buda, M. Neurock, E. Iglesia, Reactivity of chemisorbed oxygen atoms and their catalytic consequences during CH_4-O_2 catalysis on supported Pt clusters. *J. Am. Chem. Soc.* **133**, 15958–15978 (2011).
74. G.-L. Dai, Z.-P. Liu, W.-N. Wang, J. Lu, K.-N. Fan, Oxidative dehydrogenation of ethane over V_2O_5 (001): A periodic density functional theory study. *J. Phys. Chem. C* **112**, 3719–3725 (2008).
75. X. Rozanska, R. Fortrie, J. Sauer, Oxidative dehydrogenation of propane by monomeric vanadium oxide sites on silica support. *J. Phys. Chem. C* **111**, 6041–6050 (2007).
76. K. D. Campbell, J. H. Lunsford, Contribution of gas-phase radical coupling in the catalytic oxidation of methane. *J. Phys. Chem.* **92**, 5792–5796 (1988).
77. T. Ito, J. H. Lunsford, Synthesis of ethylene and ethane by partial oxidation of methane over lithium-doped magnesium oxide. *Nature* **314**, 721–722 (1985).
78. L. Luo *et al*., Gas-phase reaction network of Li/MgO-catalyzed oxidative coupling of methane and oxidative dehydrogenation of ethane. *ACS Catal.* **9**, 2514–2520 (2019).
79. C. Shi, M. P. Rosynek, J. H. Lunsford, Origin of carbon oxides during the oxidative coupling of methane. *J. Phys. Chem.* **98**, 8371–8376 (1994).
80. S. Rezgui, A. Liang, T. K. Cheung, B. C. Gates, Methane conversion to ethane in the presence of iron- and manganese-promoted sulfated zirconia. *Catal. Lett.* **53**, 1–2 (1998).
81. K. Otsuka, K. Jinno, A. Morikawa, The catalysts active and selective in oxidative coupling of methane. *Chem. Lett.* **14**, 499–500 (1985).
82. J.-L. Dubois, B. Rebours, C. J. Cameron, Oxidative coupling of methane over thoria based catalysts. *Appl. Catal.* **67**, 73–79 (1990).
83. S. J. Blanksby, G. B. Ellison, Bond dissociation energies of organic molecules. *Acc. Chem. Res.* **36**, 255–263 (2003).
84. D. L. Baulch *et al*., Evaluated kinetic data for combustion modeling. Supplement I. *J. Phys. Chem. Ref. Data* **23**, 847–848 (1994).
85. D. L. Baulch *et al*., Evaluated kinetic data for combustion modelling. *J. Phys. Chem. Ref. Data* **21**, 411–734 (1992).
86. P. Deshlahra, E. Iglesia, Reactivity and selectivity descriptors for the activation of C-H bonds in hydrocarbons and oxygenates on metal oxides. *J. Phys. Chem. C* **120**, 16741–16760 (2016).
87. K. Otsuka, M. Inaida, Y. Wada, T. Komatsu, A. Morikawa, Isotopic studies on oxidative methane coupling over samarium oxide. *Chem. Lett.* **18**, 1531–1584 (1989).
88. J. A. Labinger, K. C. Ott, Mechanistic studies on the oxidative coupling of methane. *J. Phys. Chem.* **91**, 2682–2684 (1987).
89. K. Takanabe, E. Iglesia, Rate and selectivity enhancements mediated by OH radicals in the oxidative coupling of methane catalyzed by Mn/Na2WO4/SiO2. *Angew. Chem. Int. Ed. Engl.* **47**, 7689–7693 (2008).
90. J. H. Lunsford, Catalytic conversion of methane to more useful chemicals and fuels: A challenge for the 21st century. *Catal. Today* **63**, 165–174 (2000).